Chemical Engineering Science 297 (2024) 120238

Contents lists available at ScienceDirect

Chemical Engineering Science

journal homepage: www.elsevier.com/locate/ces

Investigation of particle flow effects in slug flow crystallization using the multiscale computational fluid dynamics simulation

Shin Hyuk Kim [a,c,*], Moo Sun Hong [b], Richard D. Braatz [c,**]

[a] Department of Chemical and Biological Engineering, Hanbat National University, 125, Dongseo-daero, Yuseong-gu, Daejeon 34158, Republic of Korea
[b] Department of Chemical and Biological Engineering, 1 Gwanak-ro, Gwanak-gu, Seoul, 08826, Republic of Korea
[c] Massachusetts Institute of Technology, 77 Massachusetts Avenue, Cambridge, MA 02139, USA

ARTICLE INFO

Keywords:
Slug Flow
Crystallization
MP-PIC-PBE
Three Phase Fluids
Population Balance Equation
Computational Fluid Dynamics

ABSTRACT

This article discusses the development of a new computational fluid dynamics (CFD) model, the MVP (MP-PIC coupled with VOF and PBE) method, which predicts the slug flow crystallization phenomenon. The model is capable of predicting the flow of gas–liquid-solid phases and the associated chemical and particle changes. The MVP model is validated through a comparison with an experimental study on LAM (L-asparagine monohydrate) crystallization, and the results demonstrate its ability to accurately predict the three-phase fluid flow with particle size variation. In particular, we have been able to predict the effect of slug length change on particle mixing and predict hydrodynamic factors such as the particle streamlines and the circulation number of the particle phase via case studies. Overall, the MVP model is expected to offer a new way to accurately predict slug flow crystallization and provide valuable information for the process intensification of crystallization.

1. Introduction

The slug flow crystallizer induces the segmented well-mixed slugs using recirculation flow inside slugs that is spontaneously formed in the tubular reactor (Etminan et al., 2021; Jiang et al., 2014). The advantage of this slug production device is to realize the stable-well-mixing inside slugs without the mechanical device such as the stirred blade (Liu et al., 2021). In addition, the segmented flow tubular reactor allows a new way of stable control that, for example, the combination with spatial temperature gradient based on heat exchange sections enables particle size control through per-compartment temperature control (Mozdzierz et al., 2021). As such, in the crystallization industry, the slug flow crystallizer is spotlighted as a part of process intensification (Burns and Ramshaw, 2001).

Recently, modeling studies were introduced to utilize the slug flow reactor for crystallization (Hellmann and Agar, 2019; Mozdzierz et al., 2021; Rasche et al., 2016). A characteristic of the above studies is to assume that the mixing is perfect inside the slug. Since these studies deal with milli-fluidic or micro-fluidic, sometimes the assumption is suitable. However, the temperature and concentration inside the slug which chemical reactions take place inevitably change in space and time. In the case of crystallization, the produced crystals settle since the product has larger density than the carrier liquid phase. These features of multi-phase and multi-component flow inside the slug will disturb smooth mixing inside the slug and cause local changes in chemicals and heat. Therefore, the other modeling method is required to overcome the limitations of the perfect mixing assumption.

The CFD (computational fluid dynamics) method is useful to predict the flow effects accurately inside the slug flow reactor. For example, the VOF (volume of fluid) method (Hirt and Nichols, 1981) based on two-phase modeling is used to simulate slug flows such as a Tayler flow (Gupta et al., 2009; Gupta et al., 2010). In addition, in order to predict the slug flow with the particulate phase, it is necessary to implement the three-phase flow modeling such as liquid–liquid-solid or gas–liquid-solid. There are two model concepts for three-phase flow modeling: Euler-Euler VOF (Ngo and Lim, 2020) and Euler-Lagrangian VOF (Jing et al., 2016; Xu et al., 2013). The Euler-Euler VOF method simplifies the particulate phase as the continuous phase. Thus, the accuracy of Euler-Euler VOF method is lower than the Euler-Lagrangian VOF method which simulate the momentum of each particle. A few researches have attempted to implement the Euler-Lagrangian VOF method to predict the three-phase slug flow (Ge et al., 2020). However, these studies do

* Corresponding author at: Department of Chemical and Biological Engineering, Hanbat National University, 125, Dongseo-daero, Yuseong-gu, Daejeon 34158, Republic of Korea.
** Corresponding author at: Massachusetts Institute of Technology, 77 Massachusetts Avenue, Cambridge, MA 02139, USA
E-mail addresses: shinhyukkim@hanbat.ac.kr (S.H. Kim), braatz@mit.edu (R.D. Braatz).

https://doi.org/10.1016/j.ces.2024.120238
Received 12 December 2023; Received in revised form 3 April 2024; Accepted 12 May 2024
Available online 13 May 2024

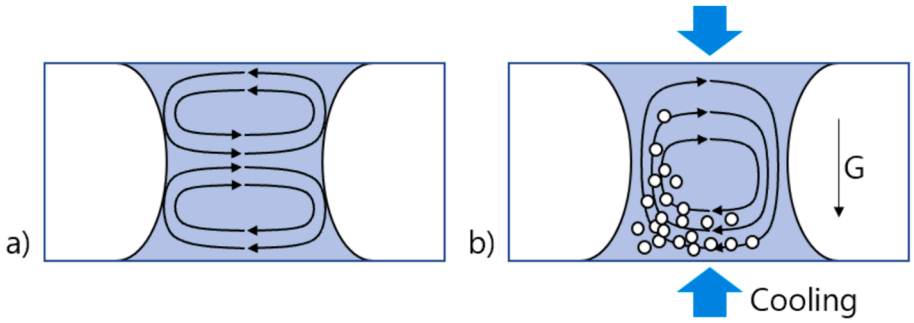

Fig. 1. Comparison of flow patterns between the a) ideal slug flow and b) slug flow for cooling crystallization.

not display the changes in chemicals and particles. Regarding the chemical changes, although Soh et al. (Soh et al., 2017) develop a CFD model that predict the mass transfer against the slug interface, the developed model is only predictable for the two-phase slug flows without the solid phase. The MP-PIC-PBE (Multiphase Particle-In-Cell coupled with Population Balance Equation) method (Kim et al., 2020, 2021) can simulate the solid phase and carrier phase flow with particle size changes, but the model cannot simulate the slug flow since the model's equations deal with only a single phase for a carrier flow. Therefore, in order to predict the slug flow crystallizer, it is required to develop a new CFD model that can handle gas–liquid-solid phases and indicate chemical changes, particle generation, and particle growth.

To this end, this study introduces a new type CFD method called MVP (MP-PIC coupled with VOF and PBE) to predict slug flow crystallization. The proposed model, different from the Euler-Lagrangian VOF method, predicts particle size change through the population balance equation and mass and heat transfer by crystallization through species balance and energy balance. The model is validated through a comparison of an actual experimental study regarding LAM (L-asparagine monohydrate) crystallization. The predicted particle phase flow patterns, and slug shape are visually compared to graphics taken by microscope cameras. In addition, the validation section compares the experimental data about particle size distribution of the end product to the simulation result. The error of the simulation result concerning the average particle size has only about 6 %. Simulation analysis results explain the characteristics of slug flows accompanied by crystallization, which could not be observed by conventional modeling methods or experimental studies. In particular, through case-studies, the effect of slug length on crystal nucleation and growth is analyzed. The investigation represents that the aspect ratio of a slug affects the particle density and the number of the particle phase re-circulations inside the slug, which in turn can change the size of the particles.

2. System description and experimental method

2.1. Slug flow for cooling crystallization

The advantage of slug flow is that it induces hydrodynamically stable mixing without external devices. Fig. 1a) shows an ideal flow pattern inside a slug. The friction on walls stops the fluid velocity against the walls and creates the fastest velocity at the center of the slug. Without gravity, the flow lines form a decalcomania-like circulation pattern (Kashid et al., 2005). This stable mixing has led many researchers to use the assumption of perfect mixing in their modeling research (Kufner et al., 2022; Mozdzierz et al., 2021; Rasche et al., 2016). However, as shown in Fig. 1b), the inside of the slug where particles are mixed causes the flow pattern to deviate from the ideal due to the gravity force. In particular, gravity acceleration is expected to be more pronounced when particles with a density about 1.5 times higher than the liquid are generated such as LAM crystallization. Additionally, external cooling can cause temperature distributions inside the slug and crystallization typically generates heat. Considering these facts, even if small slugs are used, the assumption of perfect mixing inside the slug can be inaccurate. Therefore, modeling of the slug flow crystallization needs to accurately predict particle behavior and the mixing and temperature distribution of the solution through precise flow analysis. Considering particle behavior and slug flow means concurrently dealing with the three phases of gas–liquid-solid. Moreover, the solution has a multi-component phase mixed with water and solute. Therefore, a CFD model should be able to handle the multi-component and three-phase fluid flow.

2.2. Experimental apparatus

This study analyzes the process of extracting and crystallizing L-asparagine monohydrate (LAM, purity $\geq$ 99 % (TLC)) from a solution through cooling. The experimental design is based on studies introduced by M. Jiang et al. (Jiang and Braatz, 2018; Jiang et al., 2014). The solution is prepared by mixing LAM and deionized water, and the temperature is maintained using a refrigerated temperature circulating bath with a temperature controller (CN 89202–958, from VWR) to keep the solubility below saturation. The flow rate delivered to the flask (200 ml double jacket flask) from the temperature bath is fixed, and water is used as the heat transfer fluid. The water temperature inside the bath is maintained using an electric heat source and a PI controller. The temperature of the solution is measured using a PT100 temperature sensor (combined with MAX31865, Arduino Uno, and PT100 thermocouple), and is controlled by a cascade control system that uses a PI controller (implemented using MATLAB 2022a) to maintain the temperature set point.

The reactor is a silicon tube (Masterflex L/S # HV 96400–16) with an inner diameter of 3.1 mm and an outer diameter of 6.2 mm. The slug solution and air (filtered by a polytetrafluoroethylene filter) injected into the reactor are supplied by two plastic pumps (combined with Masterflex L/S Pump Head # HV-77200–50 and Masterflex L/S Speed Console Device # 07528–30) and spontaneous slug flows are formed using a T-junction. The RPM of the air and solution pumps is adjusted to induce an aspect ratio (L/D) of 1 for the air and slug, and the flow velocity inside the reactor is maintained at 0.0345 m/s. The reactor is exposed to ambient air at a room temperature of about 21 $\pm$ 0.2 ℃, which induces the cooling down of the fluid inside the reactor.

For data measurement, the slug shape and particle flow pattern are captured using a combination of a stereomicroscope (OM4413 from OMANO) and an industrial camera with a reduction lens (DFK 42BUC03 from The Image Source, LLC, and A3RDF37 from OMAX) at approximately 7.5 m of the reactor. In addition, slug samples collected from the reactor outlet are imaged offline using a transmitted light microscope (TL3000 Ergo from Leica Microsystems). Using approximately 200 ml of solution, theoretically, about 8550 slugs can be formed. Considering the thermal stabilization time of the tube, 3 samples of slugs formed after the middle stage (around slug #4000) are empirically collected through hand-picked sampling. PSD (particle size distribution) is derived from the captured pictures through post-image processing. The image

Table 1
List of experimental conditions.

Variable	Value
Tube length	7.6 *m*
Tube inner diameter	3.1 mm
Tube outer diameter	6.2 mm
Slug velocity	0.0345 m/s
Aspect ratio (L/D) of slug shape	1
Solution concentration	0.1058 g LAM / g H_2O
Solution temperature	54 ℃ ±0.05 (327.15 K)
Room temperature	21 ℃ ±0.2 (294.15 K)

analysis procedure consists of six steps (Mozdzierz et al., 2021): 1) subtract background, 2) make binary (black and white), 3) remove noise and outliers, 4) label and split the particles in the image, 5) estimate particle objects, and 6) analyze particles. The image analysis is implemented and processed using Fiji software (source, 2023). In summary, Table 1 lists the detailed experimental conditions, and Fig. 2 shows the experimental devices.

3. MVP method description

The MVP model is a combined version of the MP-PIC-PBE and VOF models. MP-PIC-PBE can predict not only the flow of particles and carrier phases but also their chemical interactions and changes in particle size. On the other hand, the VOF model is a numerical technique for tracking and locating the free surface (or fluid–fluid interface) within CFD simulations of two or more immiscible fluids. The combination of these models enables the prediction of slug flows that require consideration of the interactions between air, solution, and particle phases. In particular, MVP can predict 1) changes in particle size, 2) mass transfer within the continuous phase, and 3) heat transfer within the continuous phase, surpassing the capabilities of existing CFD models.

3.1. Continuous flow phases

The formulas for the multiphase continuum including VOF are (1) to (9) below.

Mass equation

$$\frac{\partial(\theta_f\rho_f)}{\partial t}+\nabla\bullet\left(\theta_f\rho_f\overline{u}_f\right)=-\mathrm{S}_m \tag{1}$$

Momentum equation

$$\frac{\partial(\theta_f\rho_f\overline{u}_f)}{\partial t}+\nabla\bullet\left(\theta_f\rho_f\overline{u}_f\overline{u}_f\right)+\nabla\bullet\overline{\overline{\tau}}=-\nabla\mathrm{P}+\theta_f\rho_f\overline{g}-\overline{\mathrm{F}}+\overline{\mathrm{F}}_\sigma-\overline{u}_f\mathrm{S}_m \tag{2}$$

Volume fraction equation

$$\frac{\partial\alpha\theta_f}{\partial t}+\nabla\bullet\left(\alpha\theta_f\overline{u}_f\right)+\nabla\bullet\left(\alpha(1-\alpha)\theta_f\overline{u}_c\right)=0 \tag{3}$$

Relative velocity between solution and air phases

$$\overline{u}_c=\overline{u}_F min\left[C_F\frac{|\eta|}{|A_F|},max\left(\frac{|\eta|}{|A_F|}\right)\right] \tag{4}$$

Physical properties

$$\phi_f=\alpha\phi_s+(1-\alpha)\phi_a,\phi\in\rho,\mu,k \tag{5}$$

Continuum surface force

$$\mathrm{F}_\sigma=\sigma\kappa\nabla\alpha \tag{6}$$

Curvature

$$\kappa=-\nabla\bullet\overline{\mathrm{n}}(\theta) \tag{7}$$

Energy equation

$$\frac{\partial\left(\rho_fC_vT_f\right)}{\partial t}+\nabla\bullet\left(\rho_fC_vT_f\overline{u}_f\right)+\frac{\partial\left(\rho_fK_f\right)}{\partial t}+\nabla\bullet\left(\rho_f\overline{u}_fK_f\right)=\nabla\bullet\left[k_{eff}\nabla\mathrm{T}+\left(\overline{\overline{\tau}}_{eff}\bullet\overline{u}_f\right)\right]-\mathrm{S}_e \tag{8}$$

Species equation

$$\frac{\partial\left(\theta_fY_i\right)}{\partial t}+\nabla\bullet\left(\theta_f\overline{u}_fY_i\right)+\nabla\bullet\left(Y_i\alpha(1-\alpha)\theta_f\overline{u}_c\right)=-\mathrm{S}_{m,i}, \tag{9}$$

where θ_f is the fluid volume fraction, ρ_f is the fluid density, $\overline{u}_f$ is the fluid velocity, S_m is the mass source, $\overline{\overline{\tau}}$ is the shear stress by viscous and turbulent flow, P is the system pressure, $\overline{g}$ is the gravitational acceleration, F is the interphase momentum transfer that includes viscous drag between particles and drag force between the particulate phase and the fluid phase and shear lift force, $\overline{u}_f\mathrm{S}_m$ is the momentum source by mass transfer, α is the volume fraction of solution, $\overline{u}_c$ is the relative velocity between phases, $\overline{n}_F=A_F\bullet\nabla\alpha/|\nabla\alpha|$ is the face flux calculated from volume fraction gradient, C_F is free surface compression factor of 1, η is the volume flux, A_F is the face flux, $\phi_f,\ \phi_s,\ and\ \phi_a$ are physical properties of the fluid, solid, and air phases, F_σ is the surface tension modelled as CSF (continuum surface force)[], σ is the surface tension constant, κ is the curvature, $\overline{\mathrm{n}}(\theta)$ is the interface normal vector with a contact angle θ, C_v is the specific heat capacity of the fluid, T_f is the fluid temperature, $K_f=\left|\overline{u}_f\right|^2/2$ is the kinetic energy, k_{eff} is the fluid thermal conductivity, $\overline{\overline{\tau}}_{eff}\bullet\overline{u}_f$ is the mechanical source, S_e is the energy source by mass transfer, and Y_i is the volume fraction of component i.

The combination of the VOF method, which uses one momentum

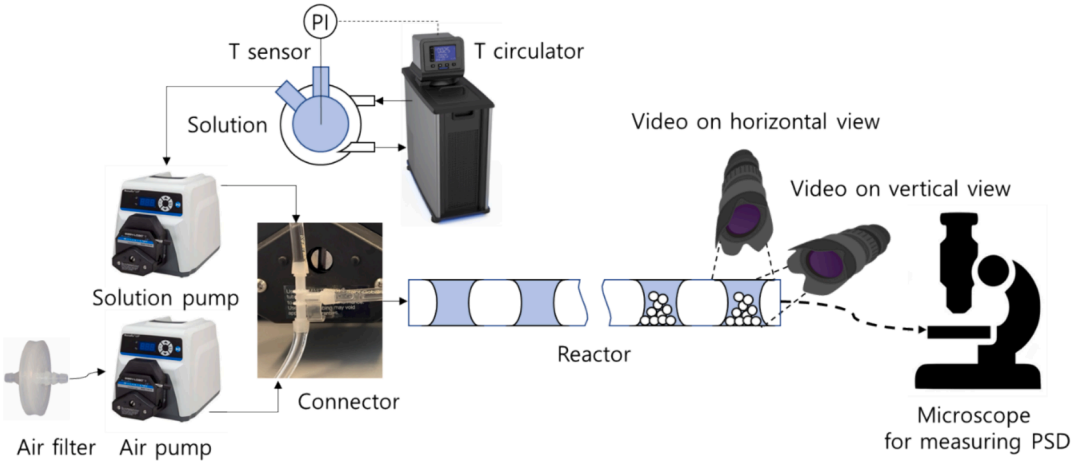

Fig. 2. Schematic of the experiment system.

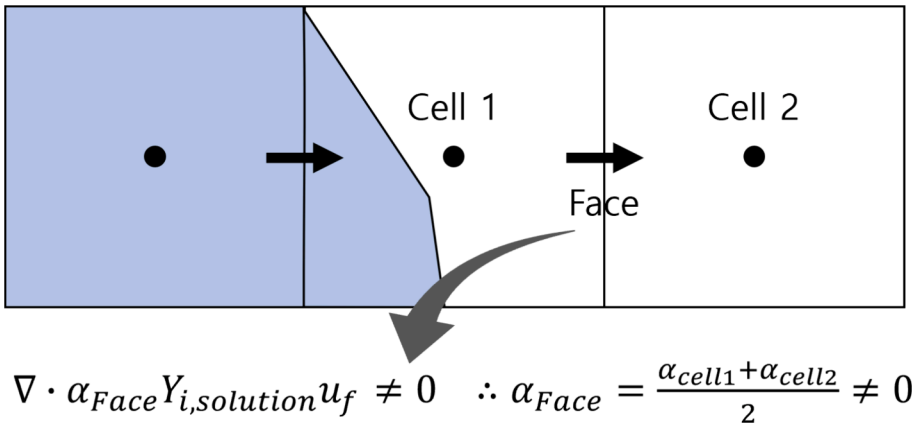

Fig. 3. Schematic showing incorrect species flux generation with VOF.

equation to represent two phases, and the species balance equation can cause inaccurate species flux at the interface (Soh et al., 2017). As shown in Fig. 3, the gradient calculation method based on the FVM (Finite Volume Method) can generate unnecessary flux in cells near the two-phase boundary. The third term of Equation (9) creates a sharper region of species at the interface, similar to the third term of Equation (3).

3.2. Particulate phase

Equation (10) ~ (17) describe dynamics of particle phase based on the MP-PIC method (Snider, 2001).

Particle distribution function

$$\frac{\partial f}{\partial t} + \nabla \bullet (f\overline{v}_p) + \nabla_{\overline{v}_p} \bullet (fA) = 0 \tag{10}$$

Particle acceleration

$$\frac{\partial \overline{v}_p}{\partial t} = \overline{\mathrm{A}} = \overline{F}_D + \overline{F}_L - \frac{1}{\rho_p}\nabla \mathrm{P} + \overline{g} - \frac{1}{\theta_p \rho_p}\nabla \tau_p \tag{11}$$

Particle drag force

$$\overline{F}_D = \mathrm{C}_d \frac{3}{8}\frac{\rho_f}{\rho_p}\frac{|\overline{u}_f - \overline{v}_p|}{r_p}(\overline{u}_f - \overline{v}_p)$$

where

$$\mathrm{C}_d = \frac{24}{\mathrm{Re}}\theta_f^{-2.65}\left(1 + 0.5\mathrm{Re}^{0.687}\right); if\ \mathrm{Re} < 1000$$

$$\mathrm{C}_d = 0.44\theta_f^{-2.65}; if \mathrm{Re} \geq 1000$$

$$\mathrm{Re} = \frac{2\rho_f|\overline{u}_f - \overline{v}_p|r_p}{\mu_f} \tag{12}$$

Particle shear lift force

$$\overline{F}_L = 6.46\rho_f \nu_f^{\frac{1}{2}} r_p (\overline{u}_f - \overline{v}_p)\left|\frac{\mathrm{d}\overline{u}_f}{dy}\right|^2 sign\left(\frac{\mathrm{d}\overline{u}_f}{dy}\right) \tag{13}$$

Isotropic interparticle stress

$$\tau_p = \frac{P_s \theta_p^{\ \beta}}{\max\{\theta_{cp} - \theta_p, \varepsilon(1-\theta_p)\}} \tag{14}$$

Particle volume fraction

$$\theta_p = \iint f \frac{m}{\rho_p} dmdv \tag{15}$$

Fluid volume fraction

$$\theta_f + \theta_p = 1 \tag{16}$$

Interphase momentum transfer function

$$\overline{F} = \iint fm\left[\overline{F}_D + \overline{F}_L - \frac{1}{\rho_p}\nabla \mathrm{P}\right] dmdv \tag{17}$$

where f is the particle distribution function in the Euler grid, $\overline{v}_p$ is the discrete particle velocity, A is the discrete particle acceleration, $\overline{F}_D$ is the particle drag function, ρ_p is the particle density, $\overline{F}_L$ is the particle shear lift function, C_d is the drag coefficient, r_p is the particle mean radius, ν_f is the kinematic viscosity of the fluid, τ_p is the interparticle stress, P_s is a constant in units of pressure, θ_p and θ_{cp} are the particle volume fraction and its maximum of 0.6, β is a constant whose value is set to 2, ε is a small number on the order of 10^{-7}, m is the total mass of the particles in a parcel, v is the volume of the mesh where a parcel is located.

3.3. Population balance equations in a parcel

The PBE that represents the particle distribution within a parcel assumed to be well-mixed is expressed in equation (18) (Kim et al., 2020). To represent cooling crystallization, the kernels consist of a nucleation rate for particle generation and a growth rate for particle growth. The slug flow reactor exhibits sufficient mixing effects without the need for external devices (Jiang et al., 2014). Therefore, breakage and agglomeration can be excluded because there is little shock applied to the particles.

$$\frac{\partial N_j}{\partial t} = -\sum_j \frac{\partial\left[G_j(r_j, S, T)\right]}{\partial r_j} + B(N_j, S, T)\prod_j \delta(r_j - r_{j0})\,. \tag{18}$$

LAM crystallization kinetics, by cooling supersaturation, consists of primary nucleation (Mozdzierz et al., 2021), and growth (Bhoi and Sarkar, 2016) as follows,

$$B(S, T) = 10^{k_{n1}} T^{\frac{1}{2}}(lnS)\exp\left[-\frac{k_{n2}}{T^3(lnS)^2}\right] \tag{19}$$

$$G(S, T) = 10^{k_{g1}}(S-1)^{k_{g2}} \tag{20}$$

$$S = \frac{M}{M_{sat}},$$

where

$$M_{sat} = 3.084 \times 10^{-2} - 1.373 \times 10^{-3}T + 5.214 \times 10^{-5}T^2 \tag{21}$$

where $k_{n1} = 9.43$ and $k_{n2} = 217$ are the necleation kinetic parameters, and $k_{g1} = -4.341$, and $k_{g2} = 1.62$ are the growth kinetic parameters, S

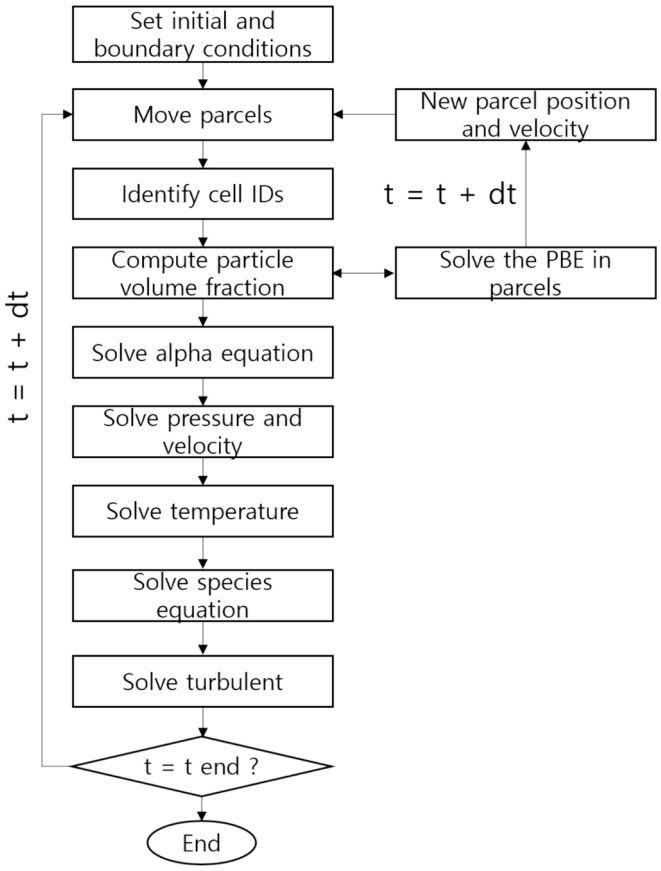

Fig. 4. Schematic diagram of the MVP model's numerical solution procedure.

is the supersaturation ratio, M is the concentration of g LAM in g water, and M_{sat} is the solubility of g LAM in g water.

The total amount and average size of particles in a parcel are calculated using equations (22) and (23), and are utilized in predicting crystallization.

$$m = V_{cell}\rho_p k_v \int r_j^3 N_j dj \tag{22}$$

$$D_{32} = \frac{\int r_j^3 N_j dj}{\int r_j^2 N_j dj} \tag{23}$$

where $k_v = 0.39551$ is the dimensionless shape factor (Mozdzierz et al., 2021).

Equation (24) represents the conversion rate of the solute, and equation (25) represents the exotherm caused by crystallization.

$$S_{m,i} = \begin{cases} \rho_p k_v \int r_j^3 \frac{\partial N_j}{\partial t} dj, i = solute \\ 0, i = water \end{cases}, \tag{24}$$

$$S_e = S_m h_{cry} \tag{25}$$

where $h_{cry} = -35700\,\mathrm{j\,mol^{-1}}$ is heat of crystallization (Rasche et al., 2016).

3.4. Numerical solution

The basic structure of the MVP is based on the MP-PIC-PBE with addition of the VOF model. The MVP model involves the detailed formulas regarding the alpha, temperature, and species equations based on the MP-PIC-PBE. The Fig. 4 shows the numerical procedure of the newly updated MVP model, and briefly describes Lgrangian phase's solution

Table 2
Equation solvers, algorithms, and tolerances.

Variable	Method	Tolerance
P	PCG + DIC	10^{-5}
u_f	PBiCGStab + DILU	10^{-8}
α	smoothSolver + GaussSeidel	10^{-12}
Turbulent (k, ω)	smoothSolver + GaussSeidal	10^{-8}
T_f	smoothSolver + GaussSeidal	10^{-10}
Y_i	smoothSolver + GaussSeidal	10^{-10}
θ_f	GAMG + GaussSeidal	10^{-6}

PCG: preconditioned gradient, PBiCGStab: stabilised preconditioned biconjugate gradient, DIC: diagonal incomplete-Cholesky, DILU: diagonal incomplete-LU, GAMG: generalised geometric-algebraic multi-grid, smoothSolver: solver that uses a smoother

Table 3
Numerical schemes.

Category	Variable or specific symbol	Method
Time	Default	Euler
Gradient	Default	linear
Divergence	Default	linearUpwind
	α, Y, T	vanLeer
	P	limitedLinear
	Turbulent	upwind
	Compression terms for Alpha and Y	linearUpwind
Laplacian	Default	Gauss linear uncorrected
Interpolation	Default	linear
Distance to wall	Default	Poisson

methods (see the Snider's research (Snider, 2001)). In order to calculate the three-phase volume transport, equation (3) and numerical schemes refer to the Jing et al. research (Jing et al., 2016). In particular, the multidimensional universal limited explicit solver (MULES) limiter (Deshpande et al., 2013) is used for guaranteeing the robustness of liquid–gas interface-tracking in large Courant number environment since the MP-PIC-PBE method requires larger mesh size than parcel volume size (Kim et al., 2020). For the solution algorithm, the pressure implicit with splitting of operator (PISO) is applied (Issa et al., 1986). Table 2 and 3 list the detailed numerical schemes which are provided options in OpenFOAM v.2106 (Ltd, 2023).

4. Description of the case study simulation

4.1. Computational domain

The geometry has been meshed as hexagonal cells using Ansys meshing module v.2022 R2 and converted to the OpenFOAM mesh format. As shown in Fig. 5, the total number of cells is about 3,500 which is decided by grid sensitivity analysis. Although the length of the domain is only 12.4 mm, which is much shorter than the actual domain of 7.6 m, a continuous tubular slug flow is simulated by implementing translational cyclic boundaries (Coe and Holland, 2023). In the case of gas–liquid slug flow, the assumption of translational periodicity is often valid because the flow patterns are repetitive and do not change significantly over the length of the tube. Particularly, in unidirectional flow, the exchange of information at the inlet and outlet boundaries relies on convective flux. Thus, even with continuous temperature and phase changes such as heat exchange with the walls and crystallization, the cyclic boundary condition can maintain the information of the accumulation of various physical variables over time within the slug. Assuming that the flux at the outlet boundary is equal to the flux at the inlet boundary, a source term, equation (25), is added to maintain the mean velocity in the flow direction at the operating velocity.

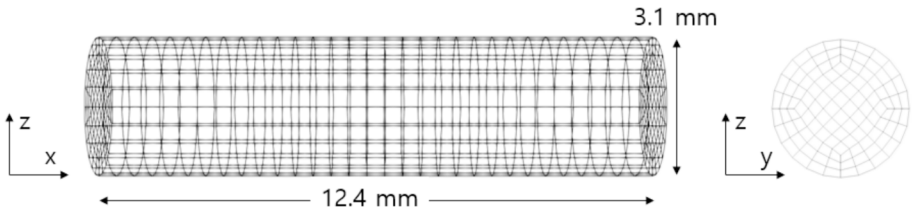

Fig. 5. Computational domain of a slug flow reactor.

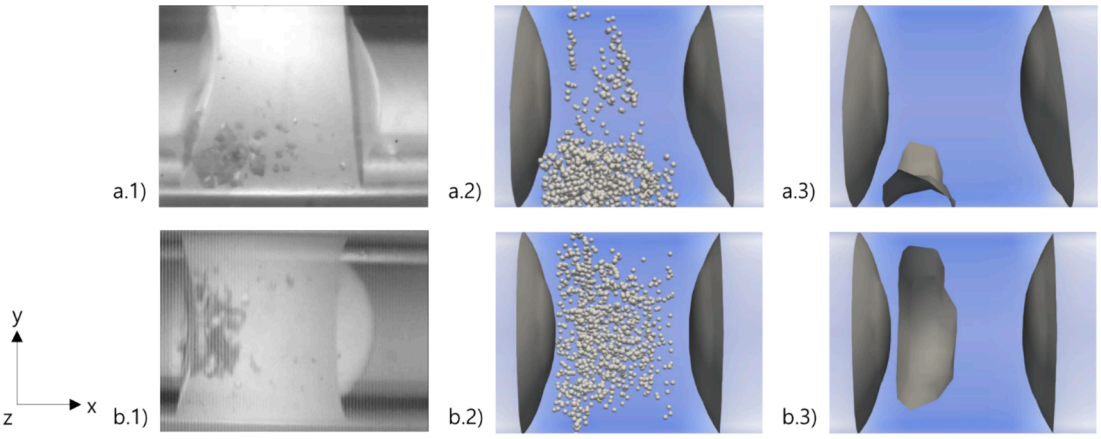

Fig. 6. Slug and particulate flow patterns captured from vertical view a), and horizontal view b). 1) is taken by a microscope camera, 2) is drawn by isolation surface of the solution volume fraction of 0.5, and tracked parcels with mean diameter of particles, and 3) is drawn by isolation surfaces of solution volume fraction of 0.5, and particle volume fraction of 0.3.

$$F_u = \frac{\|\overline{u}\| - \|\overline{u}_f\|}{a_c} \tag{25}$$

Then, the values of the two face pairs are determined via linear interpolation. The Lagrangian phase changes the x-axis coordinate to the inlet when passing through the outlet. This setup ensures mass conservation by equating the flow rate at the outlet with that at the inlet, thereby enabling the simulation of a continuous process. These cyclic boundary conditions are implemented using the cyclicAMI option provided in OpenFOAM. This simple idea allows the size of the computer domain to be reduced by about 600 times compared to the actual reactor size. A small number of meshes can significantly increase the stability and accuracy of the solution method. Time step size is adjusted according to maximum Courant number, 0.5, in each transient step. The value of the maximum Courant number has been determined by our experience to make sufficiently sharper interfaces between the solution and air phases. During the simulation, the time step size maintains about 0.0002 s. Regarding the Lagrangian phase, 1000 virtual parcels are initially injected at the inlet. The number of parcels is adjusted to match the number of cells occupied by the slug when the aspect ratio is 1.

4.2. Scenario of case studies

In order to validate the developed MVP model, the experimental conditions are applied to the simulation. To represent the heat transfer between room temperature and the slug, heat conduction between the ambient state and the tube wall, as well as heat convection between the tube wall and the inner flow, are applied (Bergman and Lavine, 2017). The velocity at the wall is assumed to be no-slip, and the k-omega model is applied to predict the small size turbulent effect to the heat transfer that can occur against the wall, despite the low Reynolds number (Wilcox, 2008). Since a cyclic boundary is used, the un-specified pressure difference (or inlet velocity) between the inlet and outlet is replaced by the mean velocity using equation (25). The slug formation due to surface tension is realized using the wall adhesion model for the wall

Table 4
Operating conditions used in the simulation.

	Variable	Value	Unit
Heat transfer at walls	Ambient temperature	21 (294.15)	℃ (K)
	Convective heat transfer coefficient (Mozdzierz et al., 2021)	20	W m^{-2} K^{-1}
	Thickness of the tube wall	0.0363	m
	Heat conductivity of the tube wall	1	m
Initial mass fraction of the LAM in a slug		0.1058	–
Initial mass fraction of the water in a slug		0.8942	–
Initial temperature		54 (327.15)	℃ (K)
Slug velocity		0.0345	m/s
Operating pressure		1	bar
AR of slugs		1, 1.5, 2, 2.5	–

Table 5
Physical properties used in the simulation.

	Variable	Value	Unit
LAM	Density	1568	kg m^3
	Heat capacity	1065	J kg^{-1} K^{-1}
	Viscosity	3.65 10^{-4}	Pa.s
	Heat of crystallization	−35700	J mol^{-1}
Water	Density	986	kg m^3
	Heat capacity	4186	J kg^{-1} K^{-1}
	Viscosity	5.47 10^{-4}	Pa.s
air	Density	Ideal gas	kg m3
	Heat capacity	1007	J kg^{-1} K^{-1}
	Viscosity	1.84 10^{-5}	Pa.s
Surface tension of the solution		0.07	N m^{-1}
Static contact angle		55	°

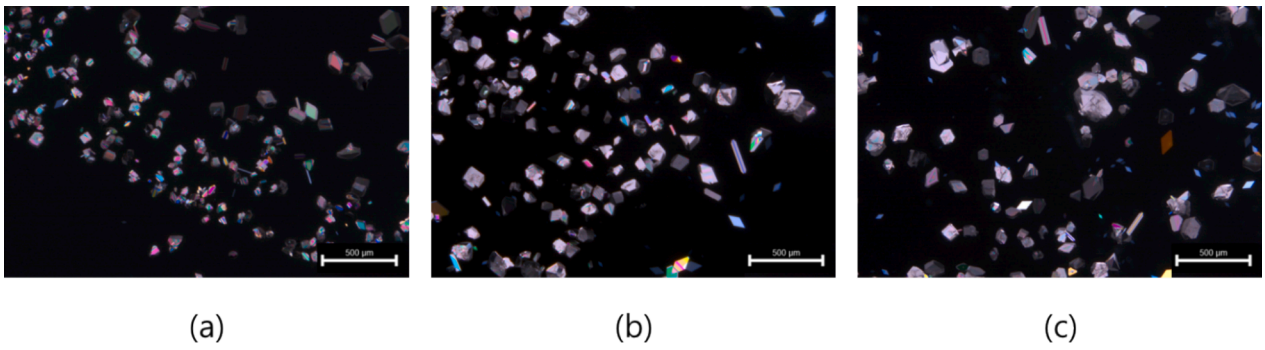

Fig. 7. Images of product crystals taken by stereo microscope: area-average crystal size through image processing (a) 79 μm, (b) 86 μm, and (c) 84 μm.

boundary condition (Brackbill et al., 1992). The wall adhesion model requires the static contact angle θ, which is experimentally measured and provided. We have found that the contact angle is approximately 55 degrees based on the image of the slug captured in Fig. 6. In summary, Table 4 summarizes the initial and boundary conditions for simulation, and Table 5 represents the physical properties required for the gas–liquid-solid phases. The gas is assumed to be a perfect mixture and ideal gas, and the liquid is assumed to be an ideal mixture of LAM and water. It is assumed that the densities of LAM and water are constant, and the viscosities and heat capacities of all phases are also constant.

Generally, modeling research on slug flow reactors assumes perfect mixing inside the slug. In this study, in order to investigate and analyze the uncertainty inherent in the perfect mixing assumption, the section 5.3 analyzes the effect of changes in the aspect ratio of the slug on particle size distribution. Considering the fact that the source of the body force of the particulate phase in slug flows depends on the attraction force by the interface between liquid and gas, it is clear that as AR increases, the circulation numbers in the particulate phase decrease during the same residence time. Therefore, the case study will produce detailed analysis results explaining the effect of particulate phase mixing on particle size growth.

5. Result and discussion

5.1. Validation

The MVP model is validated by comparing the simulation results when the AR 1 case lasts for 220 s, with photographs taken by a microscope camera at 7.5 m of the reactor. Fig. 6(a.1) shows the shape of the slug and the movement of particles inside the slug, as captured in a vertical view. The slug has a concave shape in the front and back due to surface tension, and the particles inside the slug are mostly dragged against the slug's tail and move in the x-axis direction. Some particles are carried to the front of the slug due to the strong body force formed in the center of the slug. Fig. 6(a.2) and (a.3) are graphics extracted from the simulation results through vertical section planes. The shape of the slug is drawn as an *iso*-surface using a solution volume fraction of 0.5, and the particles are represented as spheres with an average particle size of the parcel. They similarly depict the shape of the slug and particle flow pattern captured in the video. Particularly, when an *iso*-surface is drawn with a particle volume fraction of 0.3, as in Fig. 6(a.3), it is observed that most of the particles settle to the bottom of the tail of the slug due to gravity. Fig. 6b show CFD simulation results taken from a horizontal view. The settled particles gather in the center along the wall of the cylindrical tube and move in the x-axis direction pulled by the tail of the slug. As shown in Fig. 6(b.2) and (b.3), the MVP model predicts such particle behavior perfectly.

Fig. 7 shows pictures taken with a stereo microscope of three arbitrary product samples obtained at the reactor outlet. Analysis of each sample through image processing revealed that a) has an average particle size of 79 μm, b) has 86 μm, and c) has 84 μm. The average particle size of the three samples is calculated to be approximately 82 μm. The simulation of the AR 1.0 case has predicted an average particle size of around 87 μm, which is approximately 6 % larger than the average particle size obtained experimentally.

Fig. 8 compares the cumulative size distribution and the number-

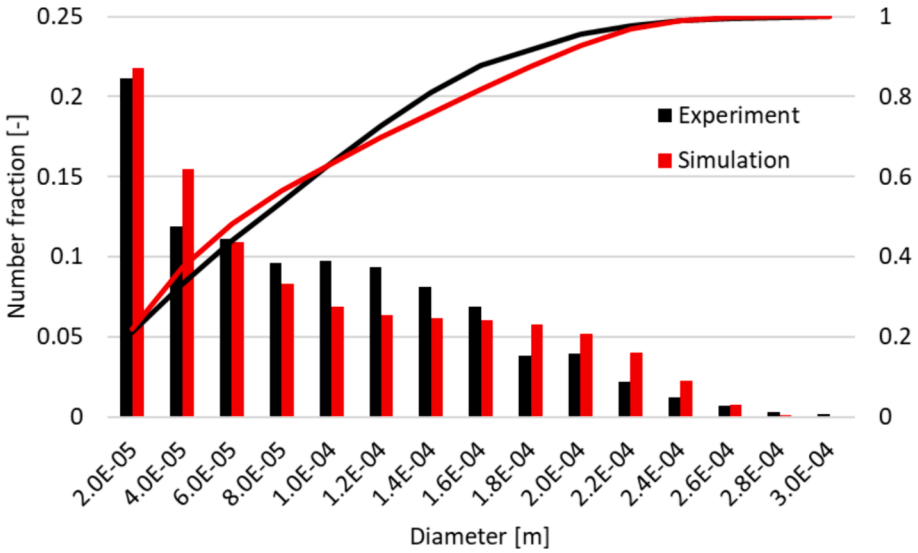

Fig. 8. Number-weighted crystal size distribution: Histogram represents number size distribution, and line represents cumulative size distribution.

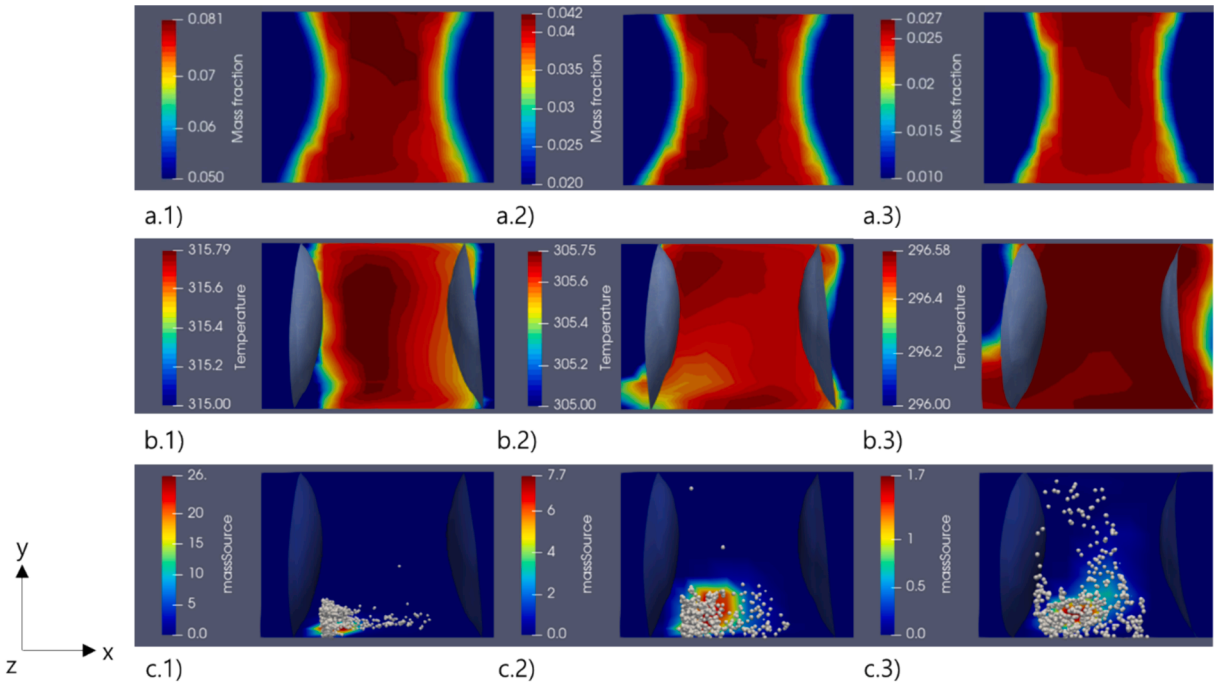

Fig. 9. Contour profiles in AR 1.0 case: a) LAM mass fraction, b) temperature, and c) crystallization rate, with time 1) 20 s, 2) 50 s, and 3) 100 s.

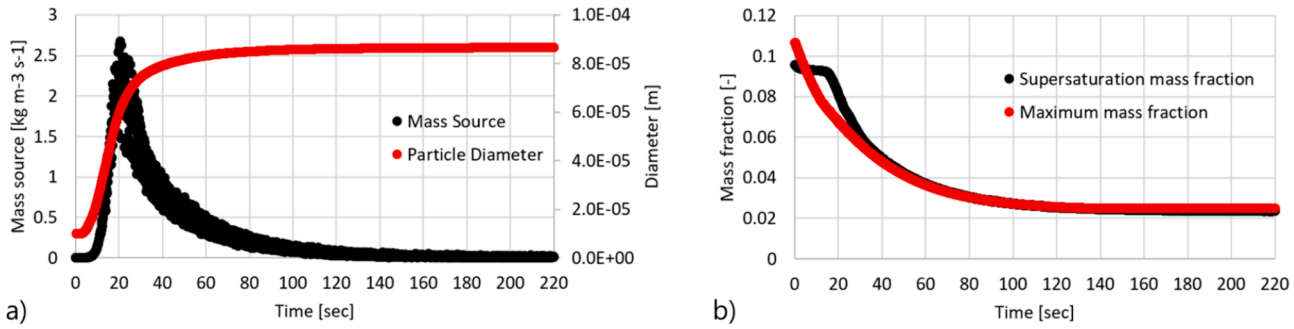

Fig. 10. Plots of CFD simulation results with time in AR 1.0 case: a) Crystallization rate (Left axis), Crystal area-average size (Right axis), and b) Supersaturation mass fraction in maximum temperature in a slug, and Maximum mass fraction of LAM in a slug.

weighted crystal size distribution obtained from the experimental results of Fig. 7 with the simulation predictions. The particle ratio in the range of 20 to 40 μm is higher in the simulation than in the experiment. In contrast, the particle ratio around 60 μm to 160 μm is higher in the experiment, and the trend reverses from 180 μm onwards. This is attributed to the fact that the Population Balance Equation (PBE) model kernels employed in our study are predicting the phenomena at a slightly slower rate compared to the actual behavior. The marginally slower nucleation and growth rates of particles are responsible for the resultant PSD that exhibits a long-tailed shape.

5.2. CFD result analysis

This section analyzes the results of time-transient simulations for the AR 1.0 case and investigates the effect of flow characteristics of slugs on crystallization. As shown in Fig. 9a, when checking the mass fraction contours of LAM inside the slug, the concentration of LAM decreases as it approaches the bottom of the slug, despite the density of LAM inside the solution is about 1.5 times higher than that of water. This is because most of the generated crystals are distributed on the bottom due to gravity, resulting in the consumption of LAM by particle growth concentrated on the bottom of the slug. Quantitatively, the difference between the maximum and minimum values of the LAM mass fraction inside the slug can be calculated as follows: 8a.1) about 0.03, 8a.2) about 0.02, and 8a.3) about 0.017 at each time period. As shown in Fig. 10a, the maximum crystallization rate is observed around 20 s, and the then crystallization rate gradually slows down, resulting in a constant average particle size from 100 s onwards. Therefore, the largest distribution difference of LAM concentration within the slug is observed around 20 s, and the concentration distribution stabilizes over time.

After the solution of 54 degree of Celsius is injected into the tube, the temperature of the slug rapidly decreases due to heat transfer with the tube wall. The rapid temperature decrease creates a temperature distribution within the slug as shown in Fig. 9b. As time goes by, if the temperature difference between the slug and room temperature decreases to a certain level, the driving force of heat transfer from the tube wall decreases, causing an occasional temperature increase due to the heat of crystallization at the slug bottom (see Fig. 9b.2)). When the temperature inside the slug decreases sufficiently to room temperature, the temperature gradient decreases, and crystallization stops, causing the temperature distribution within the slug to become constant.

Fig. 9c represents the particles' behavior and crystallization rate generated inside the slug. Since most particles are located at the bottom and tail of the slug, crystallization mainly occurs in these regions. When

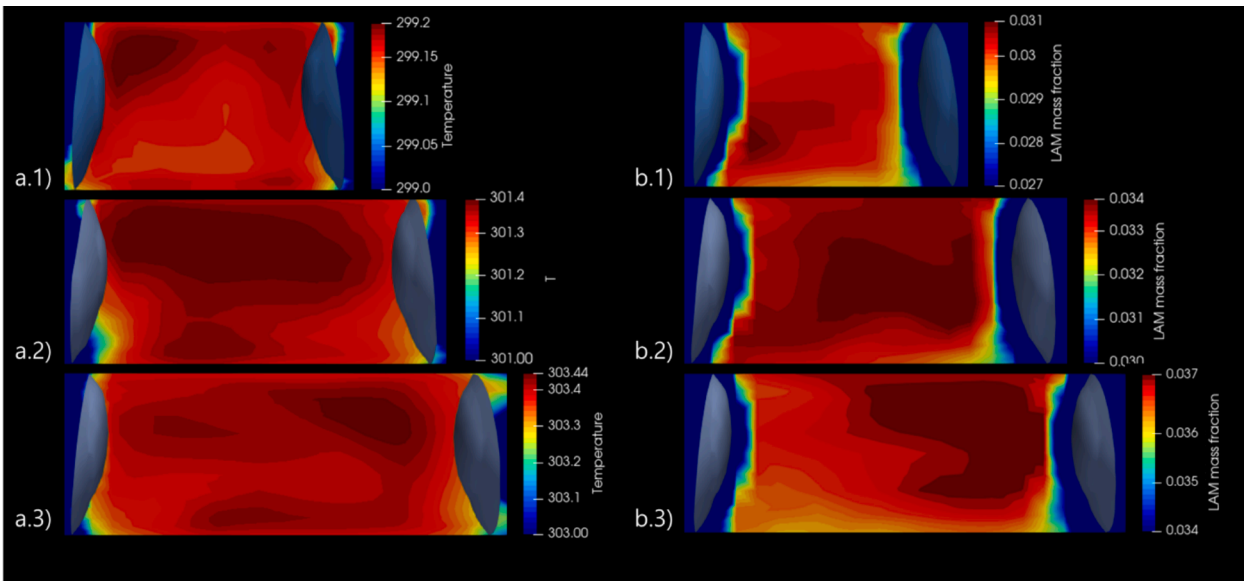

Fig. 11. Contour profiles of a) temperature, and b) LAM mass fraction in AR 1) 1.5, 2) 2.0, and 3) 2.5 cases at 100 s.

collisions between particles become frequent due to increased particle volume, as shown in Fig. 9c 3), some particles actively circulate inside the slug. Fig. 9b shows that the average supersaturation mass fraction inside the slug becomes larger than the maximum mass fraction of the slug at about 8 s as the temperature decreases after the slug is injected. The difference between the mass fraction and supersaturation mass fraction then becomes the maximum value at around 20 s (Fig. 9c 1), and Fig. 10), causing the crystallization rate to increase up to about 26.0 kg m^{-3} s^{-1} (weighted parcel number average up to about 2.7 kg m^{-3} s^{-1} as shown in Fig. 10a). As time goes by, the area where crystallization occurs increases due to the widening particle volume and movement range. However, particle generation and growth also slow down as the solvent concentration decreases. As shown in Fig. 10, since slug particle generation and growth have reached 99 % or more at around 100 s, operation for the remaining 120 s may be unnecessary. In other words, the half-length of the tube may be sufficient if the AR can be controlled to 1.0.

5.3. Effects of slug aspect ratio

The average standard deviation of the measured particle size in the experiment is approximately 2.7 μm. The disturbance influenced in the slug samples may vary. The size and number of particles generated by each slug may also differ due to the stochastic nature of the crystallization, especially nucleation. However, it has been observed clearly through a stereo microscope in experiments using transparent tube reactors that the aspect ratio of slugs varies slightly (1 to 2.5). Even when attempting to adjust the aspect ratio of slugs to match 1 using pumps and T-tubes of the same RPM, the aspect ratio of the slug sometimes becomes greater than one, or slugs may merge with other slugs while moving through the tube (Mehault et al., 2021). If the interior of the slug is assumed to be perfectly mixed, then theoretically, the particle generation should not be affected by different aspect ratios. In other words, the assumption of perfect mixing will be valid. However, if the interior of the slug is not thoroughly mixed, the perfect mixing assumption may be

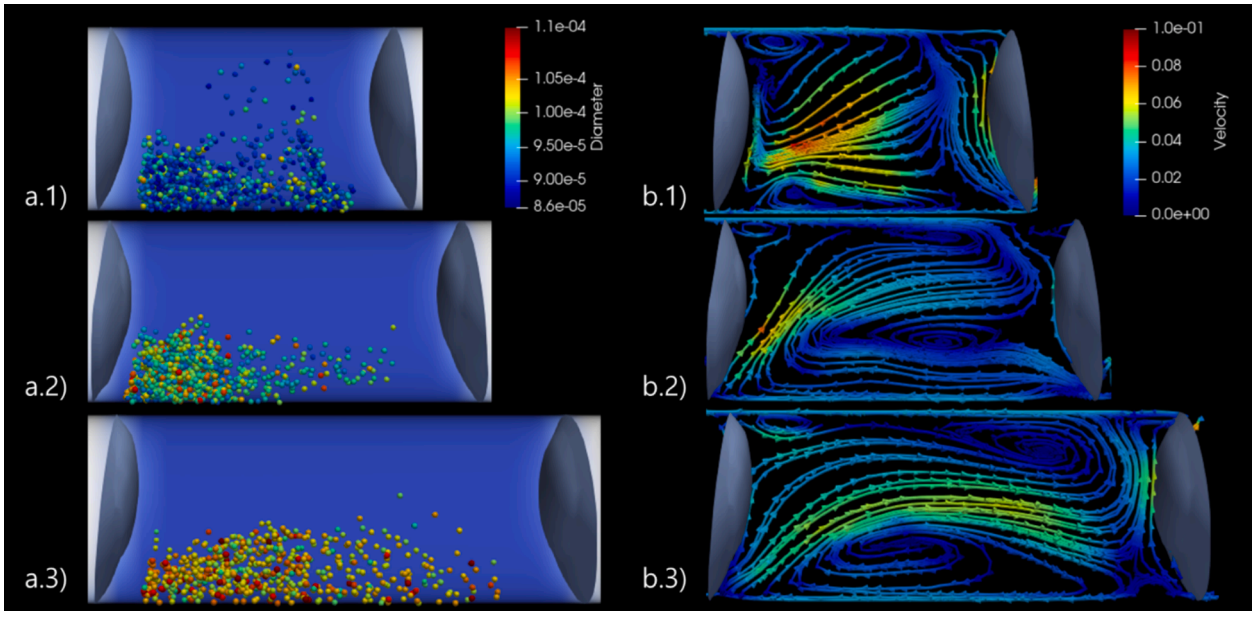

Fig. 12. A) particle size and particle flow patterns, and b) relative velocity ($\overline{u} - \overline{u}_f$) and streamlines in AR 1) 1.5, 2) 2.0, and 3) 2.5 cases at 100 s.

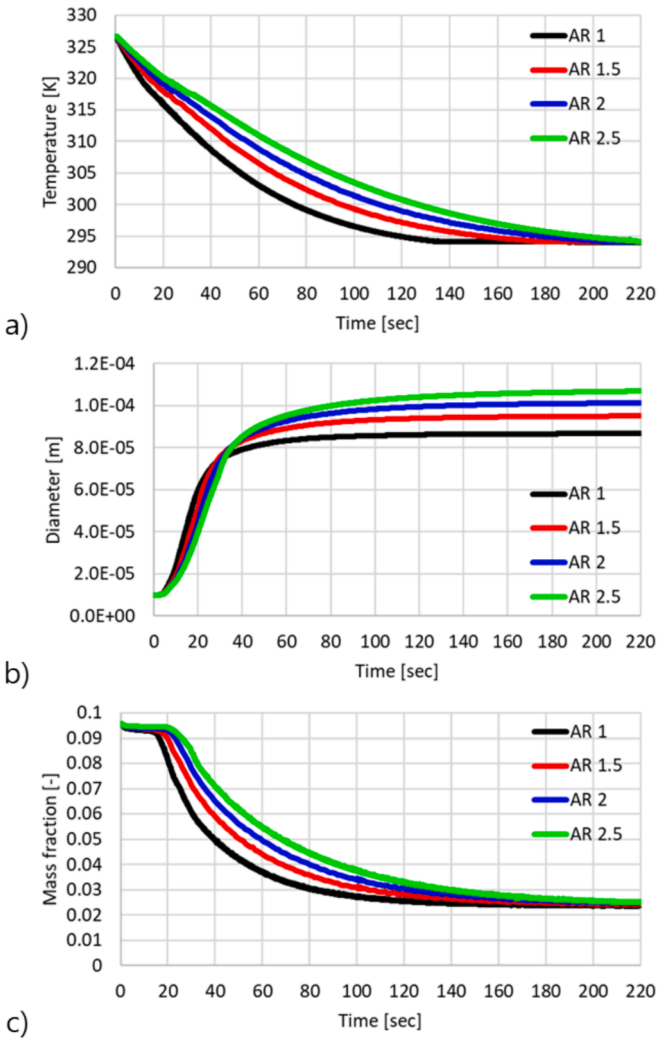

Fig. 13. Plots of CFD simulation results with time from AR 1.0 to 2.5 case: a) Maximum temperature in a slug, b) Crystal area-average size, c) Maximum mass fraction of LAM in a slug.

incorrect. Therefore, this section investigates whether the assumption of a perfect mixing reactor is still valid by predicting the temperature, concentration, particle size, and flow pattern inside the slug when the aspect ratio is different.

Fig. 11 describes contour profiles of temperature and LAM mass fraction in the vertical section planes of the slug. These graphics compare the slug's state inside when the slug's AR is different at a residence time of 100 s. In the temperature results, the larger the AR, the higher the temperature of the slug at the same residence time because when the AR of the slug increases, the heat loss decreases as the ratio of the increase in the heat transfer area to the increase in the slug's volume. Therefore, when using the same cooling system, the temperature decrease rate of the slug slows down as the slug's AR increases. When observing the temperature distribution inside the slug, it appears that the temperature decreases more quickly in the lower part of the slug than in the upper part. As shown in Fig. 12a, the flow pattern of the particulate phase vigorously moving on the bottom by gravity makes the main flow pattern inside the slug dependent on one large recirculation zone, as shown in Fig. 12b. Although A small upper recirculation zone still exists, a large recirculation zone at the bottom of the slug distributes the temperature well at that location, creating a temperature distribution inside the slug. In addition, quantitatively, the temperature deviation inside the slug increases as the AR increases (see Fig. 11a.1) = ~0.07 K, 11a.2) = ~0.12 K, and 11a.3) = ~0.14 K). It seems that the

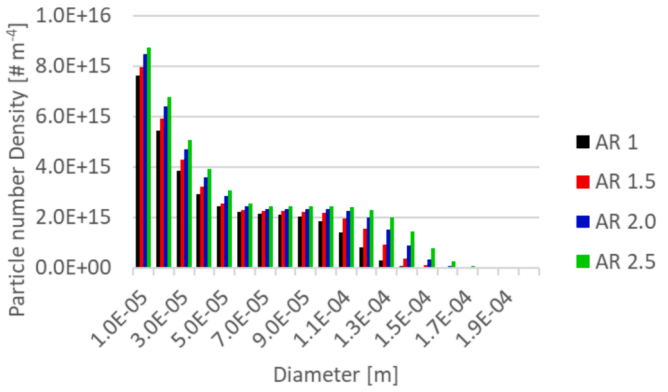

Fig. 14. Comparison of crystal size distribution predicted in case studies.

heat mixing ability inside the slug decreases as the slug becomes longer. Fig. 12 can be good evidence for this opinion. As shown in Fig. 12a, particles can be circulated well even with an increasing AR. However, Fig. 12b represents that the central body force that moves particle forward in the slug gradually decreases as the AR increase (u_{max} = ~0.10 m s^{-1} at AR 1.5, u_{max} = ~0.08 m s^{-1} at AR 2.0, and u_{max} = ~0.05 m s^{-1} at AR 2.5). As a result, when the AR increases, the velocity at the center of the slug is lowered, and the particles' circulation frequency decreases as the slug's length increases, thereby lowering the mixing force inside the slug.

The LAM mass fraction of the slug solution still shows a lower value in the lower part, even when the AR changes, as shown in Fig. 11b. This is because most particles move while settled, and they use LAM as they grow, even when the AR increases.

Fig. 13 shows the temperature, average particle diameter, and maximum mass fraction of LAM over time in a slug as AR changes. As shown in Fig. 13a, the slug needs more time to cool as the AR increases, causing the activation of crystallization to be delayed. A slowdown in the rate of LAM concentration reduction due to AR changes does not mean a slowdown in particle nucleation and growth. Even if the initial particle growth rate decreases as AR increases due to the decrease in cooling rate (see Fig. 13b), a large volume of slug induces supersaturation by a temperature drop while maintaining a high lam concentration, resulting in larger particle growth (see Fig. 13c). Due to the sensitivity of solubility to concentration according to equation (21), higher LAM concentrations can induce stronger crystallization. Additionally, higher LAM concentrations impact particle growth more than nucleation. Therefore, as AR increases, the average particle size increases.

Fig. 14 illustrates the variations in particle distribution with changes in the Aspect Ratio (AR). Initially, an increase in AR is observed to correlate with an augmentation in the total number of particles generated. Furthermore, the capability to sustain a high concentration has facilitated the significant growth of particles. In essence, slugs with a larger AR have not only produced particles of a greater average size but have also quantitatively generated a larger and more substantial number of particles.

6. Conclusion

This research introduces a newly developed CFD numerical procedure, the MVP method, to investigate the slug crystallization phenomenon. The developed method can predict the three-phase fluid flow with particle size variation, which could not be shown by existing CFD models, and its ability is verified through comparison with experimental results.

The validation is performed in two stages. First, the flow pattern of the slug captured by a camera in the experiment is qualitatively compared with the CFD results. Second, the particle size distribution obtained by image processing from the end product, which is captured

by a stereo microscope, is compared with the simulation results. The CFD simulation results have represented the flow pattern of particles sinking to the bottom of the reactor and the shape of the slug, which has been consistent with the images captured in the experiment. The model has also predicted the average particle size with an error of about 6 %. Furthermore, the MVP model has revealed that the flow pattern of sinking particles causes the distribution of temperature, concentration, and crystallization rate in the slug and explains it physically and chemically. These verification results indicate that the MVP model can be useful for simulating particle movement inside the actual reactor.

In the case studies, the MVP model predicts that the size and number of particles formed can change depending on the size of the slug. The simulation results clearly explain that the slug size is one factor that interrupts the actual experimental setup from producing particles of the same size every time. For example, an increase in AR from 1.0 to 2.5 leads to a larger slug volume, slower temperature reduction, larger temperature and concentration distribution, and lower frequency of particle circulation, which reduces nucleation due to cooling and increases particle growth rate due to the increased LAM concentration. As a result, the size of the particles can increase as the AR increases. These findings clearly depict the limitations of the perfect mixing assumption for slug flow crystallization modeling. This investigation result suggests that slug AR is a variable that must be controlled in the development of slug flow crystallizers in the future, and that perfect mixing may be a poor assumption.

In the future, we will complement the MVP model and focus on intensification research on the slug flow crystallizer through the MVP model. For example, we will complement the PBE kernels used in the MVP model, add secondary nucleation reflecting the spatial distribution of particles, and attempt parameter estimation based on the MVP model to improve the model accuracy. In addition, the MVP model will be used in research to control particle size by manipulating the flow pattern on slug crystallization or changing the size or shape of the tube to control particle size.

CRediT authorship contribution statement

Shin Hyuk Kim: Writing – original draft, Software, Project administration, Methodology, Investigation, Data curation, Conceptualization. **Moo Sun Hong:** Methodology, Formal analysis, Conceptualization. **Richard D. Braatz:** Writing – review & editing, Supervision, Methodology, Conceptualization.

Declaration of competing interest

The authors declare that they have no known competing financial interests or personal relationships that could have appeared to influence the work reported in this paper.

Data availability

No data was used for the research described in the article.

Acknowledgement

This work was supported by the National Research Foundation of Korea (NRF) grant funded by the Korea Government (No. NRF-2021R1C1C2012717).

References

Bergman, T.L., Lavine, A., 2017. Incropera's principles of heat and mass transfer, Global, 8th ed. Wiley, Hoboken, N.J.
Bhoi, S., Sarkar, D., 2016. Modelling and experimental validation of ultrasound assisted unseeded batch cooling crystallization of L-asparagine monohydrate. CrstEngComm 18, 4863–4874.
Brackbill, J.U., Kothe, D.B., Zemach, C., 1992. A continuum method for modeling surface-tension. J. Comput. Phys. 100, 335–354.
Burns, J.R., Ramshaw, C., 2001. The intensification of rapid reactions in multiphase systems using slug flow in capillaries. Lab Chip 1, 10–15.
Coe, M., Holland, D., 2023. A Cyclic Heat Transfer Solver for OpenFOAM. OpenFOAM® Journal 3, 225-251.
Deshpande, S.S.A., Lakshman, Trujillo, M.F., 2013. Evaluating the performance of the two-phase flow solver interFoam. Comput. Sci. Discov. 5, 014016.
Etminan, A., Muzychka, Y.S., Pope, K., 2021. A review on the hydrodynamics of taylor flow in microchannels: experimental and computational studies. Processes 9, 870.
Ge, L.H., Peng, Z.B., Moreno-atanasio, R., Doroodchi, E., Evans, G.M., 2020. Three-dimensional VOF-DEM model for simulating particle dynamics in the liquid slugs of a vertical gas-liquid-solid taylor flow microreactor. Ind. Eng. Chem. Res. 59, 7965–7981.
Gupta, R., Fletcher, D.F., Haynes, B.S., 2009. On the CFD modelling of Taylor flow in microchannels. Chem. Eng. Sci. 64, 2941–2950.
Gupta, R., Fletcher, D.F., Haynes, B.S., 2010. Taylor flow in microchannels: a review of experimental and computational work. The Journal of Computational Multiphase Flows 2, 1–31.
Hellmann, D., Agar, D.W., 2019. Modeling of slug velocity and pressure drop in gas-liquid-liquid slug flow. Chem. Eng. Technol. 42, 2138–2145.
Hirt, C.W., Nichols, B.D., 1981. Volume of fluid (vof) method for the dynamics of free boundaries. J. Comput. Phys. 39, 201–225.
Issa, R.I., Gosman, A.D., Watkins, A.P., 1986. The computation of compressible and incompressible recirculating-flows by a noniterative implicit scheme. J. Comput. Phys. 62, 66–82.
Jiang, M., Braatz, R.D., 2018. Low-cost noninvasive real-time imaging for tubular continuous-flow crystallization. Chem. Eng. Technol. 41, 143–148.
Jiang, M., Zhu, Z.L., Jimenez, E., Papageorgiou, C.D., Waetzig, J., Hardy, A., Langston, M., Braatz, R.D., 2014. Continuous-flow tubular crystallization in slugs spontaneously induced by hydrodynamics. Cryst. Growth Des. 14, 851–860.
Jing, L., Kwok, C.Y., Leung, Y.F., Sobral, Y.D., 2016. Extended CFD-DEM for free-surface flow with multi-size granules. Int. J. Numer. Anal. Meth. Geomech. 40, 62–79.
Kashid, M.N., Gerlach, I., Goetz, S., Franzke, J., Acker, J.F., Platte, F., Agar, D.W., Turek, S., 2005. Internal circulation within the liquid slugs of a liquid-liquid slug-flow capillary microreactor. Ind. Eng. Chem. Res. 44, 5003–5010.
Kim, S.H., Lee, J.H., Braatz, R.D., 2020. Multi-phase particle-in-cell coupled with population balance equation (MP-PIC-PBE) method for multiscale computational fluid dynamics simulation. Comput. Chem. Eng. 134, 106686.
Kim, S.H., Lee, J.H., Braatz, R.D., 2021. Multi-scale fluid dynamics simulation based on MP-PIC-PBE method for PMMA suspension polymerization. Comput. Chem. Eng. 152, 107391.
Kufner, A.C., Krummnow, A., Danzer, A., Wohlgemuth, K., 2022. Strategy for fast decision on material system suitability for continuous crystallization inside a slug flow crystallizer. Micromachines 13, 1795.
Liu, Y.Y., Zhao, Q.K., Yue, J., Yao, C.Q., Chen, G.W., 2021. Effect of mixing on mass transfer characterization in continuous slugs and dispersed droplets in biphasic slug flow microreactors. Chem. Eng. J. 406, 126885.
Ltd, O., 2023. OpenFOAM.
Mehault, C., Vanoye, L., Philippe, R., de Bellefon, C., 2021. Multiphase alternated slug flows: Conditions to avoid coalescence and characterization of mass transfer between droplets. Chem. Eng. J. 407, 127215.
Mozdzierz, N.J., Lee, Y., Hong, M.S., Benisch, M.H.P., Rasche, M.L., Tropp, U.E., Jiang, M., Myerson, A.S., Braatz, R.D., 2021. Mathematical modeling and experimental validation of continuous slug-flow tubular crystallization with ultrasonication-induced nucleation and spatially varying temperature. Chem. Eng. Res. Des. 169, 275–287.
Ngo, S.I., Lim, Y.I., 2020. Multiscale Eulerian CFD of chemical processes: a review. Chemengineering 4, 23.
Rasche, M.L., Jiang, M., Braatz, R.D., 2016. Mathematical modeling and optimal design of multi-stage slug-flow crystallization. Comput. Chem. Eng. 95, 240–248.
Snider, D.M., 2001. An incompressible three-dimensional multiphase particle-in-cell model for dense particle flows. J. Comput. Phys. 170, 523–549.
Soh, G.Y., Yeoh, G.H., Timchenko, V., 2017. A CFD model for the coupling of multiphase, multicomponent and mass transfer physics for micro-scale simulations. Int. J. Heat Mass Transf. 113, 922–934.
source, o., 2023. Fiji.
Wilcox, D.C., 2008. Formulation of the k-omega Turbulence Model Revisited. AIAA J. 46, 2823–2838.
Xu, Y.G., Liu, M.Y., Tang, C., 2013. Three-dimensional CFD-VOF-DPM simulations of effects of low-holdup particles on single-nozzle bubbling behavior in gas-liquid-solid systems. Chem. Eng. J. 222, 292–306.